Inorganic Chemistry

Article

pubs.acs.org/IC

# Original Synthetic Route To Obtain a $SrAl_2O_4$ Phosphor by the Molten Salt Method: Insights into the Reaction Mechanism and Enhancement of the Persistent Luminescence

Rocío Estefanía Rojas-Hernandez,*[,†] Fernando Rubio-Marcos,[†] Ricardo Henrique Gonçalves,[‡] Miguel Ángel Rodriguez,[†] Emmanuel Véron,[§] Mathieu Allix,[§] Catherine Bessada,[§] and José Francisco Fernandez[†]

[†]Electroceramic Department, Instituto de Cerámica y Vidrio, CSIC, Kelsen 5, 28049, Madrid, Spain

[‡]Departments of Chemistry and Materials Engineering, Federal University of Sao Carlos, 13565-905 Sao Carlos, SP, Brazil

[§]CNRS, CEMHTI UPR3079, University of Orléans, F-45071 Orléans, France

Supporting Information

**ABSTRACT:** $SrAl_2O_4:Eu^{2+}$, $Dy^{3+}$ has been extensively studied for industrial applications in the luminescent materials field, because of its excellent persistent luminescence properties and chemical stability. Traditionally, this strontium aluminate material is synthesized in bulk form and/or fine powder by the classic solid-state method. Here, we report an original synthetic route, a molten salt assisted process, to obtain highly crystalline $SrAl_2O_4$ powder with nanometer-scale crystals. The main advantages of salt addition are the increase of the reaction rate and the significant reduction of the synthesis temperature because of much higher mobility of reactants in the liquid medium than in the solid-state method. In particular, the formation mechanism of $SrAl_2O_4$, the role of the salt, and the phase's evolution have been explored as a function of temperature and time. Phosphorescent powders based on $SrAl_2O_4:Eu^{2+}$, $Dy^{3+}$ with high crystallinity are obtained after 1 h treatment at 900 °C. This work could promote further interest in adopting the molten salt strategy to process high-crystallinity materials with enhanced luminescence to design technologically relevant phosphors.

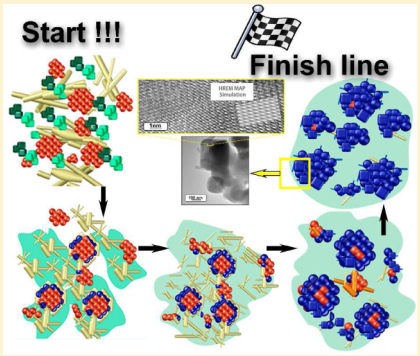


## 1. INTRODUCTION

Owing to its excellent phosphorescence properties and good stability,[1−4] $SrAl_2O_4$ has attracted increasing interest as a candidate material for a wide field of applications as persistent luminous paints, inks, ceramics, etc.[5−7] Much attention has been paid to the development of efficient methods for the preparation of $SrAl_2O_4$ powders, including the sol−gel method, hydrothermal synthesis, chemical precipitation, laser synthesis, combustion synthesis, and solid-state reaction.[8−14] Many of these techniques are not compatible with large-scale production and with the principles of sustainability. Moreover, industrial availability of highly crystalline powders usually requires high synthesis temperatures, typically between 1300 and 1900 °C, with long processing times, especially for solid-state reactions.[15] As a result, the average particle size is typically within the 20−100 $\mu$m range.[16−18] This large particle size limits the performance of actual applications such as coating, luminescent labels for bioimaging,[19] and printing.

New approaches are required to overcome these synthesis limitations. The sol−gel method has been employed to reduce the synthesis temperature. For example, by the sol−gel methodology based on a Pechini's method modification and adding $B_2O_3$, $SrAl_2O_4:Eu^{2+},Dy^{3+}$ powders have been obtained at 1200 °C; however the grain size is around 45 $\mu$m.[9,18] Moreover, as reported in a different study, in spite of decreasing the average grain size to 50−90 nm, it is necessary to use a multistep process, i.e., burning at 600° and sintering at 1100−1400 °C, and the luminescence intensity of the nanograde is much lower than that of the micrometer grade.[20] From these results, it appears that novel methods are required to overcome actual limitations. The molten salt process possesses relevant advantages over the previous methods for the synthesis of strontium aluminates, the main one being that synthesis in flux is potentially interesting to obtain high crystallinity and therefore large luminescent response. Furthermore, the molten salt method decreases the reaction temperature and reduces the reaction time.[21]

In this method the raw materials are mixed together with a salt; then the mixture is heat treated to a temperature higher than the melting point of the salt.[22] The molten salt fluxes have been employed to enhance the reactivity and promote crystal growth in systems such as complex oxides powders: $BaZrO_3$,[23] $KSrNb_5O_{15}$,[24] $ZnAl_2O_4$.[25] The molten salt process has similarities to single crystal prepared by the seeded method but extended to particle synthesis. Nevertheless, only little

Received: July 23, 2015
Published: October 8, 2015

  

DOI: 10.1021/acs.inorgchem.5b01656
Inorg. Chem. 2015, 54, 9896−9907

information has been reported regarding the mechanisms of the reaction assisted by molten salts. This reaction is mainly described by a combination of two mechanisms: "dissolution−precipitation" and "template formation".[21] The former implies the dissolution of the reactants in the molten salt, followed by the formation of the reaction product and at the end of the process the precipitation of the product. While the latter implies the dissolution of one reactant, this component is transported to the other reactant and the product is formed on the surface of this last reactant. However, the mechanism is unclear and not well addressed. Generally speaking, the molten salts behave as an ionic liquid in which the dissolution of a metal cation is very limited.[26,27] Thus, the strong and promising advantages of the molten salt method are frustrated by the lack of knowledge in the field.

A key parameter in the molten salt method is the nature of the molten salt flux. There are some requirements for the nature of the salt that must be fulfilled, such as an adequate melting point, good chemical stability, easy washability, and low cost. Each system demonstrates a different behavior, so it is important to precisely determine the heat treatment and the kind and the amount of salt required. Chlorides and sulfates are typically used in many applications.[28−32] Due to their low melting point, nitrate salts are also studied, but synthesis reactions behave differently compared to chloride or sulfate systems.[33] Concerning the amount of salt to be used, it is usually between 80% and 120% of the weight of the reactant mixture, or using the molar ratio of the salt/complex oxide (S/O), S/O = 1:1, 3:1, 4:1, 5:1, or 20:1, depending on the nature of the product and the salt.[21]

To date, $SrAl_2O_4$ synthesis by the molten salt method has not been reported in the literature. The hydraulic activity of the aluminates impedes removal of the remaining salt by water washing, and, probably, this fact has discouraged further exploration of this process. However, this method has been employed by Zhang et al.[25,34] in other systems such as $MgAl_2O_4$ and $ZnAl_2O_4$. The authors reported the synthesis of these materials using LiCl, KCl, and NaCl as molten salts, and they observed a decrease of the synthesis temperature compared to the conventional solid-state powder process. The formation mechanism was depicted by the template mechanism, previously mentioned.

The purpose of this article is to understand the mechanisms of the molten salt assisted process for strontium aluminate particles. The kinetics of the reaction and its influence on the $SrAl_2O_4$ phase formation of submicrometer particles are studied. Interestingly, the material obtained by this process presents strong crystallinity and intense luminescence compared to the classic synthesis methods. These achievements could have an important influence on the ability to obtain crystalline particles with enhanced optical properties.

## 2. EXPERIMENTAL DETAILS

**Synthesis.** $SrAl_2O_4:Eu^{2+}$, $Dy^{3+}$ particles were synthesized by molten salt synthesis. In all the experiments, the raw materials were first dried at 120 °C for 1 h due to their hygroscopic nature. $Sr_{1-x-y}Eu_xDy_yAl_2O_4$ compositions with $x = 0.02$ and $y = 0.01$ were prepared using $Al_2O_3$ (Almatis, specific suface area, BET: 13 $m^2/g$, average particle size, $d_{50} \approx 0.1$ $\mu$m), $SrCO_3$ (Merck, 99.9%, $d_{50} \approx 1.1$ $\mu$m), $Eu_2O_3$ (Metal Rare Earth Limited, 99.5%, $d_{50} \approx 3.8$ $\mu$m), and $Dy_2O_3$ (Rare Earth Limited, 99.5%, $d_{50} \approx 3.1$ $\mu$m) as precursors. The molten salt was composed of a mixture of NaCl (99.5% purity) and KCl (99.5% purity) using a 0.5:0.5 molar ratio (eutectic mixture hereafter abbreviated as $(NaCl−KCl)_e$). It was dry homogenized by grinding in a 60 $cm^3$ nylon container for 20 min by using a Turbula mixer at 50 rpm with $ZrO_2$ balls with a diameter of 0.5 mm. The above materials were mixed in the same dry conditions using the Turbula mixer. The salt/$SrAl_2O_4$ molar ratio was kept at 3:1. The homogenized mixture was placed in an alumina crucible with a platinum foil to avoid reaction with the crucible. The powders were heated to a given temperature in air atmosphere and held for 1 h in order to study the mechanisms. For the study of the phosphor properties the thermal treatment was held in a $90N_2−10H_2$ atmosphere. A white powder was finally obtained.

**Structural and Microstructural Characterization.** Thermogravimetric analysis−differential scanning calorimetry (ATG−DSC) analyses were carried out on a Perkin−Elmer DSC-7 equipment under an air atmosphere from room temperature (RT) to 1100 °C using a heating rate of 10 °C $min^{-1}$.

The crystalline phases were characterized by X-ray diffraction (XRD, D8, Bruker) using a Lynx Eye detector and Cu $K\alpha_{1,2}$ radiation. Quantitative phase analysis was performed using the Rietveld method and the General Structure Analysis System (GSAS) program with the EXPGUI graphical user interface.[35,36]

*In situ* high-temperature X-ray diffraction data were collected using a D8 Advance Bruker Bragg−Brentano diffractometer equipped with a Vantec-1 linear detector and an HTK1200N Anton Paar oven chamber based on a Kanthal resistive heating attachment. The sample was deposited on a platinum disk in an alumina crucible. The temperature behavior and thermal expansion of the setup were previously calibrated using the corundum reference.[37] The sample was heated from RT to 750 °C at a rate of 10 °C $min^{-1}$, and the ramp was stopped for each diffractogram to avoid any change during the data collection. For this experiment, the maximum temperature was fixed at 750 °C to avoid equipment damage due to vaporization of the salt in the heating chamber.

The Raman study was carried out using a confocal Raman microscopy instrument (Witec ALPHA 300RA with Nd:YAG laser excitation at 532 nm and a 100× objective lens (NA = 0.9)). The incident laser power was 19.6 mW. The optical diffraction resolution of the confocal microscope was limited to about 200 nm laterally. Raman spectral resolution of the system was down to 0.02 $cm^{-1}$. The microscopy sample was mounted in a piezo-driven scan platform having a 4 nm lateral accuracy. Samples were deposited on a microscopy glass slide. Collected spectra were processed and analyzed by using Witec Control Plus software 2.08. The Raman mapping consisted of 1600 simple spectra of 2 s of integration time each.

HRTEM and EDX analyses were performed to obtain detailed phase composition and morphological characterization. A TECNAI F20 FEI microscope was used, operating at 200 kV. HRTEM simulations were performed via the multislice method[38] using the JEMS software package.[39]

**Luminescent Characterization.** Optical properties of these materials were investigated by measuring emission and excitation spectra. The photoluminescence spectra of the phosphor particles were recorded with a spectrofluorometer (Fluorolog-3, HORIBA Jobin Yvon) at room temperature. The emission spectrum was measured over the wavelength 400−700 nm; a Xenon arc lamp was used as an excitation source ($\lambda_{exc}$ = 380 nm). The decay profiles were also recorded using the same instrument after the samples were exposed to $\lambda_{exc}$ = 380 nm for about 10 min.

## 3. RESULTS AND DISCUSSION

**3.1. Reaction Mechanism by Thermal Analysis Studies.** The selection of the salt highly depends on its stability and solubility in water after the reaction process. The salt ought not to generate undesirable reactions neither with the reactants nor with the final product. Additionally, the salt should have a low melting point in order to obtain the target phase. Consequently, the eutectic composition is often used, as its melting point is considerably lower than the melting points of the pure phases. Taking into account these requirements, the


DOI: 10.1021/acs.inorgchem.5b01656
Inorg. Chem. 2015, 54, 9896−9907

eutectic mixture of NaCl and KCl, $(NaCl–KCl)_e$, has been selected.[21]

In order to investigate the behavior of the salt $(NaCl–KCl)_e$ and the salt in contact with the raw materials, a detailed thermal study was carried out and is shown next.

*$(NaCl–KCl)_e$.* DSC-TG-DTG curves of the $(NaCl–KCl)_e$ heated to 1100 °C at a rate of 10 °C $min^{-1}$ in air are shown in Figure 1a. A sharp endothermic peak is observed at 659 °C

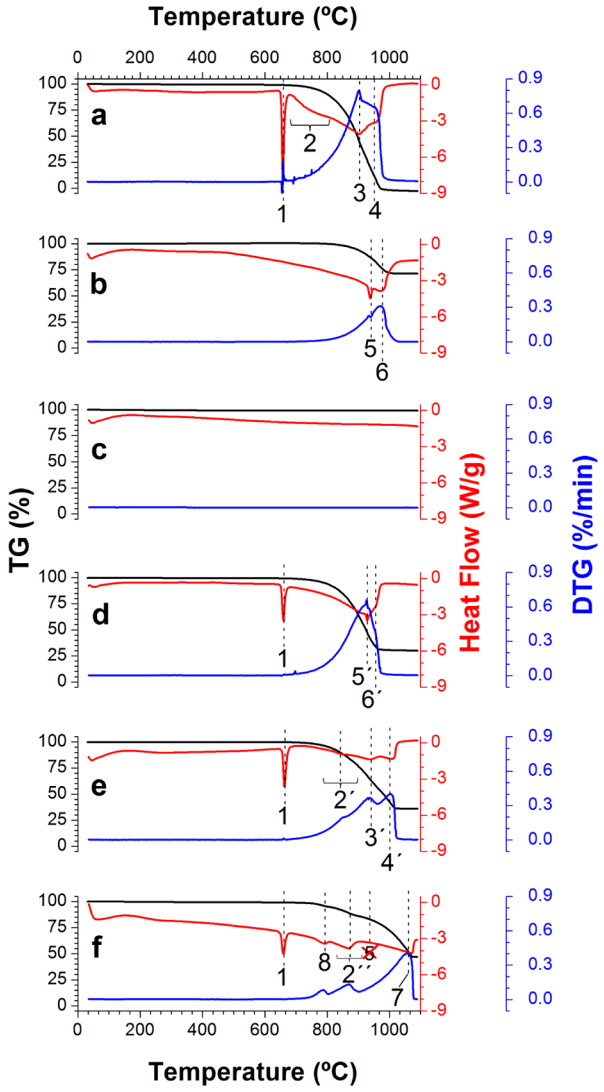


**Figure 1.** Thermal analysis: DSC-TG-DTG curves of the precursor materials (a) eutectic salt mixture $(NaCl–KCl)_e$, (b) $SrCO_3$, and (c) $Al_2O_3$. DSC-TG-DTG curves of the systems: (d) $SrCO_3$ + $(NaCl–KCl)_e$, (e) $Al_2O_3$ + $(NaCl–KCl)_e$, and (f) $SrCO_3$ + $Al_2O_3$ + $(NaCl–KCl)_e$ heated to 1100 °C at a 10 °C $min^{-1}$ rate. The numbers next to the peaks represent endothermic and/or exothermic processes that occurred during the thermal analysis on the different systems.

(peak signal 1 in Figure 1a); this peak can be ascribed to the melting point of the eutectic mixture.[40] The endothermic peaks at 690–800 °C (2 in Figure 1a) are due to the presence of pure salts in the melt. Some solid particles of NaCl and KCl are not fully incorporated into the eutectic liquid. For this reason, a higher temperature is required to dissolve the pure phases. At higher temperature, the evaporation of the salt mixture occurs. The broad peaks observed at 903 and 954 °C (3 and 4 in Figure 1a) can be interpreted as the vaporization of KCl and NaCl, respectively, due to some grains of NaCl and KCl that remain pure. It should be noted that a molten salt is an ionic liquid, and its behavior can be understood with the concept of vapor pressure: the salt can decompose thermally or vaporize as a salt at lower temperatures than its boiling point.[26,41] The 100% weight loss of the eutectic mixture occurs at ca. 1010 °C.

*$SrCO_3$ + $(NaCl–KCl)_e$ and $Al_2O_3$ + $(NaCl–KCl)_e$.* Figure 1b and c show the DSC-TG-DTG of $SrCO_3$ and $Al_2O_3$, respectively. The endothermic peak at 938 °C of the DSC analysis of $SrCO_3$ is attributed to the phase transition from the orthorhombic to the hexagonal $SrCO_3$ polymorph (peak 5 in Figure 1b). Then, the decomposition of the carbonate happens at ca. 1013 °C (6 in Figure 1b). Regarding the DSC-TG-DTG of $SrCO_3$ and $(NaCl–KCl)_e$ mixing (Figure 1d), it can be observed that the position of the peak ascribed to the melting point of the eutectic mixture does not change (see the peak marked as 1 in Figure 1d). This is because the salt does not interact with the oxide and is kept as molten flux. Nevertheless, the evaporation of the salt is completed at higher temperatures with $SrCO_3$ incorporation, while the thermal decomposition of the carbonate is lowered from 1013 °C to 983 °C (6′ in Figure 1d). Moreover, the peak at 938 °C related to $SrCO_3$ transformation from orthorhombic to hexagonal is also shifted to lower temperature (927 °C, peak 5′ in Figure 1d). This can be explained by the fact that DSC is a dynamic analysis, and the phase transformation remains visible because the carbonate is not totally decomposed by the molten salts.

The system $Al_2O_3$ + $(NaCl–KCl)_e$ also shows a delayed vaporization that can be attributed to the reduction of the surface tension by the presence of solid particles (Figure 1e). The presence of three endothermic peaks can be observed between 800 and 1000 °C. The peak at 853 °C (2′ in Figure 1e) is more noticeable with respect to the peak in the DSC of the salt, given that $Al_2O_3$ decreases the diffusion of NaCl and KCl in the liquid phase. Moreover, the endothermic peaks at 937 and 1000 °C (3′ and 4′ in Figure 1e) are related to KCl and NaCl vaporization, which shift to higher temperature in comparison to the pure salt.

*$SrCO_3$ + $Al_2O_3$ + $(NaCl–KCl)_e$.* The behavior of the system is better described by analyzing the DSC-TG-DTG of $SrCO_3$ + $Al_2O_3$ + $(NaCl–KCl)_e$ (Figure 1f). It is noticeable that the phase transformation peak of $SrCO_3$ disappears. This can be explained by the presence of $Al_2O_3$, which drastically lowers the thermal decomposition of the carbonate as observed by Chang et al.[42] As previously discussed, the peak corresponding to the evaporation of KCl is shifted from 903 °C to 937 °C with addition of alumina. However, no peak is observed from 900 to 1000 °C when $SrCO_3$ is also added. Therefore, the absence of this peak could be due to the inclusion of $SrCO_3$, which probably promotes the diffusion of KCl through the molten salt. The endothermic peak located at 1070 °C (7 in Figure 1f) is shifted due to the decrease of the mobility of NaCl. Moreover, the addition of $SrCO_3$ decreases the diffusion of NaCl and KCl in the liquid (broad peak signal 2″ in Figure 1f), given that the peak at 852 °C in $Al_2O_3$ + $(NaCl–KCl)_e$ moves to 865 °C in the $SrCO_3$ + $Al_2O_3$ + $(NaCl–KCl)_e$ system. This assumption is correlated with the extinction of the peak corresponding to the evaporation of KCl, because the delay of diffusion of NaCl and KCl in the liquid allows all the incorporation of KCl, avoiding an evaporation stage of this pure salt. On the other hand, a new endothermic peak appears at 789 °C (peak marked as **8** in Figure 1f); this peak can be attributed to the formation of the tridymite structure ($SrAl_2O_4$).



DOI: 10.1021/acs.inorgchem.5b01656
*Inorg. Chem.* 2015, 54, 9896–9907

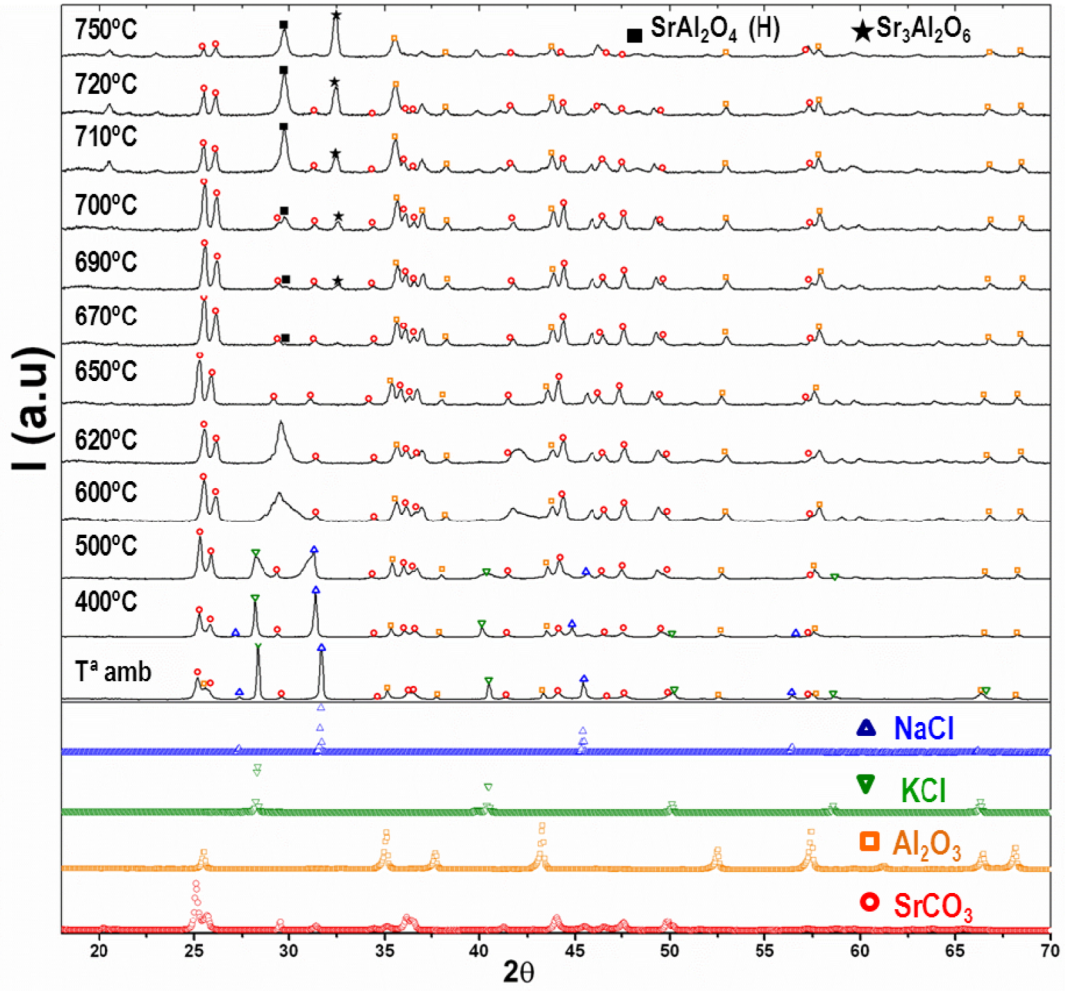


**Figure 2.** Evolution of *in situ* XRD patterns collected upon heating (10 °C $min^{-1}$) from 25 to 750 °C. The reference diffraction patterns of raw materials are shown at the bottom. The symbols highlight $SrCO_3$ (red open circles), $Al_2O_3$ (orange open squares), NaCl (green open triangles), and KCl (green open triangles).

To sum up, according to the thermal measurements performed in the system, the melt salt $(NaCl–KCl)_e$ mixed with $Al_2O_3$ seems to promote the decomposition of $SrCO_3$. Moreover, the salt improves the chemical reactivity on the solid by increasing the atomic mobility of $Sr^{2+}$. It is known that the dissociation energy of SrO is lower than that of $Al_2O_3$; therefore $Sr^{2+}$ diffusion prevails in comparison with $Al^{3+}$.[43,44]

**3.2. Kinetic Study by *in Situ* HT-XRD.** In order to identify the transformation of the crystalline phases during the reaction process, the results obtained by thermal analysis were completed by *in situ* HT-XRD experiments. Figure 2 shows the X-ray diffractogram evolution upon heating the $SrCO_3$ + $Al_2O_3$ + $(NaCl–KCl)_e$ system from room temperature up to 750 °C. For each phase, we focused our study on a main peak that did not overlap with any other phase in order to accurately follow their evolution. Moreover we checked the absence of preferred orientation, which would have interfered with the intensity evolution, by comparison with the theoretical intensities.

The identification of the crystalline phases was carried out using the International Centre for Diffraction Data (ICDD) database. As expected, the diagram collected at room temperature presents the characteristic peaks of the $SrCO_3$ (JCPDF file 74-1491), $Al_2O_3$ (JCPDF file 73-1512), NaCl (JCPDF file 72-1668), and KCl (JCPDF file 76-3376) raw materials. At around 500 °C, a broadening of the reflections related to NaCl and KCl is observed, corresponding to the amorphization of the salt. On the diagram collected at 600 °C, the appearance of new large peaks located at ∼29.6°, 42°, and 52° ($2\theta$) reveals the formation of the $Na_xK_{1-x}Cl$ (JCPDF file 75-0295) solid solution with a limited degree of crystallinity (small crystallite size). Only the reflections ascribed to $SrCO_3$ and $Al_2O_3$ crystalline phases are visible at 650 °C due to the complete melting of the salts.

From a temperature of 670 °C to the end of the thermal treatment, two new main peaks are rising at $2\theta \approx 29°$ and 32°, while the intensity of the reflections of $SrCO_3$ tends to decrease slowly. This change can be attributed to the formation of a $SrAl_2O_4$ hexagonal polymorph (JCPDF file 31-1336) and $Sr_3Al_2O_6$ (JCPDF file 24-1187) at the expense of strontium carbonate. The broadening of the reflections observed on the powder diffraction data indicates that $SrAl_2O_4$ and $Sr_3Al_2O_6$ crystallize in small domains. In the literature, the crystallization of $SrAl_2O_4$ is reported to take place at 850 °C, after 1 h of solid-state reaction,[42] and at 900 °C after holding the temperature for 1 h and starting from sol–gel synthesis.[9] The results obtained by *in situ* HT-XRD measurements confirm that the molten salt eases diffusion in the system and promotes the formation of



DOI: 10.1021/acs.inorgchem.5b01656
*Inorg. Chem.* 2015, 54, 9896–9907

strontium aluminate phases. It is worth noting that the reaction stage starts just above the melting temperature of the salt, measured at 659 °C by thermal analysis. Apart from the ability of the salt to improve the diffusion, the nature of $Al_2O_3$ influences also the reaction mechanism. The $Al_2O_3$ precursor employed in this study is more reactive in comparison with a conventional $\alpha$-$Al_2O_3$; furthermore it has a large specific surface area (BET: 13 $m^2/g$), which leads to a greater contact between particles, thus promoting the phase reaction. The formation of $Sr_3Al_2O_6$ suggests that an excess of $SrCO_3$ takes place locally, which promotes the formation of this rich strontium compound in the melt.

Additionally, it is important to remark that $SrAl_2O_4$ has two polymorphs depending on the temperature: below 650 °C the monoclinic form is stable, and above this temperature $SrAl_2O_4$ crystallizes in hexagonal symmetry. For this reason, the peaks observed during the experiment are correlated to the hexagonal phase. Some authors reported that only the monoclinic structure doped with rare earth ions exhibits luminescent properties.[45,46] However, Jia et al.[47] suggested that the hexagonal $SrAl_2O_4$ polymorph has higher emission efficiency than the monoclinic polymorph.

The simultaneous formation of $SrAl_2O_4$ and $Sr_3Al_2O_6$ suggests that there is not enough time to promote the decomposition of $SrCO_3$ during the *in situ* experiments. For this reason, $Sr_3Al_2O_6$ appears in addition to $SrAl_2O_4$ for short thermal treatments.

**3.3. Phase Formation of $SrAl_2O_4$ Studied by Raman Spectroscopy.** In order to follow the reaction as a function of temperature and the holding time, the powders were isothermally treated at 670, 700, 800, and 900 °C for 1 h. These temperatures between 670 and 900 °C were chosen to set the reaction just above the melting point (659 °C) and to understand the strontium aluminate formation increase with the synthesis temperature. Confocal Raman microscopy has been used for monitoring the phase evolution. In order to distinguish the raw material evolution with the temperature, it is imperative to first depict the Raman spectra of these raw materials (Figure 3). From previous $SrCO_3$ studies by Raman

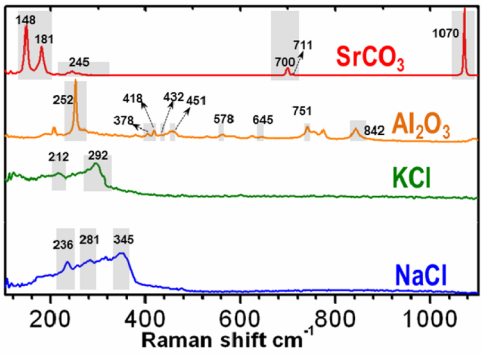


**Figure 3.** Raman spectra of raw $SrCO_3$, $Al_2O_3$, NaCl, and KCl powder at room temperature.

spectroscopy,[48−50] 30 Raman-active modes can be predicted. Nevertheless the spectrum acquired in this study shows fewer modes. The spectra are governed by Raman lines at 148 and 181 $cm^{-1}$ attributed to the angular oscillations and at 1070 $cm^{-1}$ attributed to the symmetric stretching mode ($\nu_1(A'_1)$) of the carbonate group $(CO_3)^{2-}$. The low-intensity Raman mode visible at 245 $cm^{-1}$ is ascribed to the external vibration modes between the cation and anionic group (T(Sr, $CO_3$)) and at 700 and 711 $cm^{-1}$ to the symmetric bending mode of the carbonate group, respectively. Concerning $Al_2O_3$, it has been reported that $\alpha$-$Al_2O_3$ (corundum) is based on $D^6_{3d}$ symmetry with seven Raman-active phonon modes, $2A_{1g} + 5E_g$, at frequencies of 378, 418, 432, 451, 578, 645, and 751 $cm^{-1}$.[51]

Referring to the Raman characterization of the salts, NaCl shows an asymmetric Raman mode at 345 $cm^{-1}$ and two Raman modes at 236 and 281 $cm^{-1}$. These Raman modes are related to acoustical and optical modes of NaCl.[52] On the other hand, KCl shows the characteristic alkali halite Raman modes at 212 and 292 $cm^{-1}$.[53] The intensity of the Raman modes corresponding to the salts has a lower signal than other phases; therefore it has not been possible to distinguish these Raman modes in the thermally treated samples.

The Raman study has been carried out by means of surface (XY) Raman images of the powder isothermally treated at 670, 700, 800, and 900 °C during 1 h, which correspond to Figure 4a−d, respectively. These Raman images show a color-coding indicating the region of the sample where the Raman spectrum corresponds to the one presented in Figure 4e. Therefore, the surface Raman image provides information about the spatial distribution of the different phases as a function of the thermal treatment.

The Raman image of the powder thermally treated at 670 °C, presented in Figure 4a, shows four distinguishable phases. The Raman image is governed by the presence of carbonate groups. There are defined regions clearly correlated with strontium carbonate (yellow region and yellow Raman spectrum shown in Figure 4a and e, respectively), and all Raman spectra possess the carbonate group in addition to the different Raman modes for each phase. The carbonate group is thus distributed in the whole area of the Raman image. This fact indicates that strontium is partially incorporated in the melt salt but remains unreacted. $Al_2O_3$, which is signaled by red regions, remains relatively dispersed in agglomerates of 2−4 $\mu$m in size (Figure 4a and e). It is an indication that the alumina particles are not affected by the presence of the molten salt. The average Raman spectrum representing large regions (pink region of Figure 4a) is composed by two main Raman modes, 478 and 418 $cm^{-1}$. The first Raman mode is attributed to the formation of $SrAl_2O_4$, whereas the second one belongs to unreacted $Al_2O_3$. To date, only a few Raman studies deal with the tridymite-like $AB_2O_4$ compound, and it lacks complete Raman peak assignation. However, the Raman mode at 465 $cm^{-1}$ has been reported[9,54] as the bending of O−Al−O bonds in corner-sharing tetrahedra, for pure $SrAl_2O_4$ powders with great crystallinity. Accordingly, the presence of the peak around 478 $cm^{-1}$ exhibits the formation of $SrAl_2O_4$ in the powders treated at 670 °C, and the Raman blue-shift indicates a higher constant force for this bond. It is important to remark that there is coexistence of both the hexagonal and monoclinic $SrAl_2O_4$ phases at this stage. As in the hexagonal phase the cation packing is higher, and the shortening of the bonds indicates the correlation of this Raman blue-shift with the presence of strontium aluminate in hexagonal symmetry. Therefore, the Raman band corresponding to the bending of O−Al−O bonds may be related to both phases, and it is difficult to unequivocally assign this Raman peak to the monoclinic or to the hexagonal phase at this stage because of their incipient formation. The incipient formation of strontium aluminate is observed joined with the Raman mode $A_{1g}$ at 418 $cm^{-1}$, corresponding with $Al_2O_3$. This result shows the


DOI: 10.1021/acs.inorgchem.5b01656
*Inorg. Chem.* 2015, 54, 9896−9907

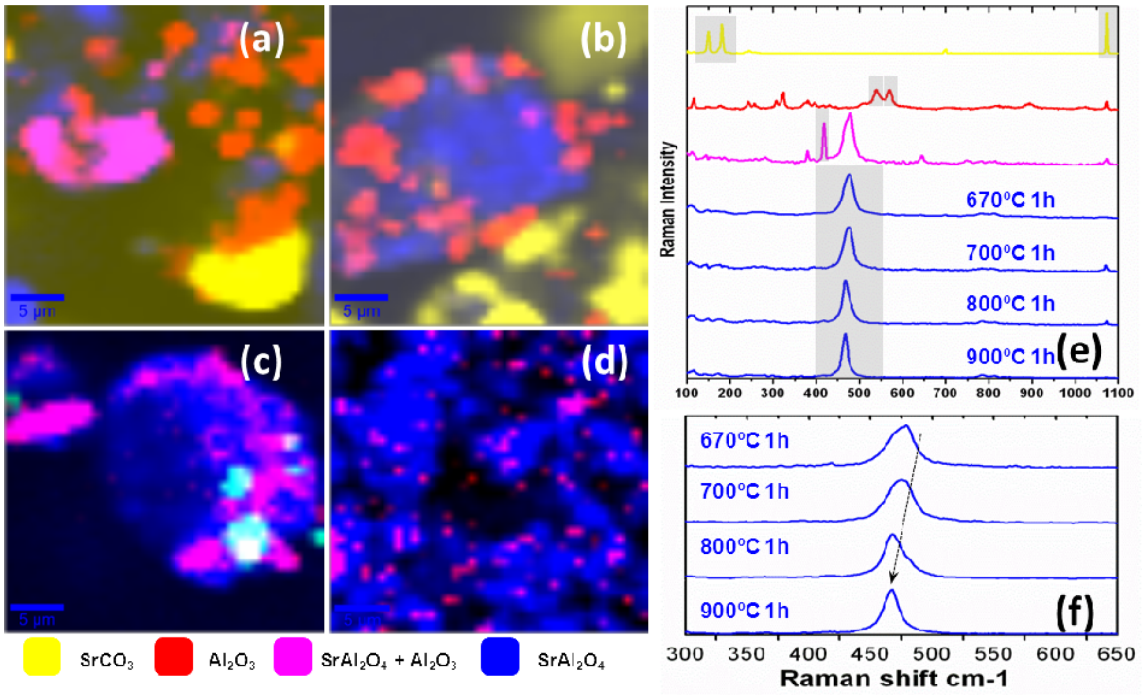


**Figure 4.** Raman images of the phase spatial distribution for powders thermally treated at (a) 670, (b) 700, (c) 800, and (d) 900 °C for 1 h. (e) Average Raman spectra correspond to each phase; the color-coded Raman spectrum corresponds with the color-coded areas in the Raman images. (f) Magnified Raman spectra in the range from 300 to 650 $cm^{-1}$ of average Raman spectra of the blue regions for powders treated at different temperatures. The arrow marks the red-shift of the Raman peak.

coexistence in the same region of both $SrAl_2O_4$ and unreacted $Al_2O_3$. In some regions, the reaction is complete, as signaled by the absence of the Raman mode $A_{1g}$ at 418 $cm^{-1}$ (blue regions). It is worth noting that the presence of alumina particles near strontium carbonate does not promote the formation of strontium aluminate because the latter does not decompose. The incipient formation of $SrAl_2O_4$ is related to the presence of a limited amount of strontium cation in the molten salts that remains in their carbonate state at this temperature.

The average Raman spectrum of the blue regions of the powders treated at different temperatures is shown at the bottom of Figure 4e. The present phases and their distribution after thermal treatment at 700 °C are given in Figure 4b. The amount of $SrAl_2O_4$ increases and the unreacted alumina and strontium carbonate particles remain present in the Raman image. Increasing the temperature to 800 and 900 °C, Figure 4c and d, leads to a large increase of the reaction so that the amount of $SrCO_3$ becomes nearly insignificant. The absence of pure $Al_2O_3$ regions indicates that the reaction is generalized. Unreacted $Al_2O_3$ always coexists with $SrAl_2O_4$, and the size of these regions diminished with the temperature increase. The presence of $SrAl_2O_4$ shown by the *in situ* HT-XRD results correlates with the presence of enlarged regions (Figure 4c,d).

On the basis of the analysis of the Raman fingerprints, the system appears to have almost completely converted into $SrAl_2O_4$ when $SrCO_3$ is decomposed and unreacted $Al_2O_3$ is reduced to small regions always in coexistence with the $SrAl_2O_4$ phase. These findings suggest that the strontium aluminate particles could possess an unreacted $Al_2O_3$ core. Figure 4f illustrates a detail of the region between 300 and 650 $cm^{-1}$, as a function of the thermal treatment. It is clearly observed that a red-shift of the bending of O−Al−O occurs for higher thermal treatment temperatures. In addition, the full width at half-maximum (fwhm) clearly decreases. In a first approach, possible explanations accounting for such a behavior could be (i) the crystalline size enlarges or (ii) the structure transforms into a more open crystalline structure as the monoclinic phase. The first approach is consistent with the expected increasing in size of particles with a higher temperature treatment. For the second approach it may be considered that the Raman analysis is performed at RT and that $SrAl_2O_4$ transforms from the high-temperature hexagonal polymorph to the low-temperature monoclinic phase. This fact implies that to some extent the hexagonal phase could be stabilized at RT. Moreover, it can also be observed that the Raman band is more asymmetric and broad at 670 and 700 °C, and the coexistence of both hexagonal and monoclinic phases could also be expected. In order to elucidate such a behavior, a deep analysis of the crystalline structure is required.

### 3.4. Corroborating $SrAl_2O_4$ Formation by RT-XRD.

Following the above analysis and in order to obtain quantitative information, the Rietveld refinement method has been applied on powder diffraction data obtained at room temperature from samples treated at 670, 700, 800, and 900 °C for 1 h (Figure 5). The background was fitted with a linear interpolation function with 36 coefficients. The peak profiles were refined using one theta independent Gaussian term and two Lorentzian coefficients, Lx(1/cos, crystal size broadening) and Ly(tg, microstrain broadening), of a pseudo-Voigt function.[55] Unit cell parameters, scale factors, displacement, and zero-shift correction parameters were also refined. The results of the phase quantification and the figures of merit (Rwp factor, $\chi^2$, and $R(F^2)$) for each refinement are compiled in Table 1. In addition, visual results of the plots show the accomplishment of the Rietveld refinement, as reflected by the small difference between calculated and observed diagrams.

The results of the quantitative phase analysis clearly show that the $SrCO_3$ and $Al_2O_3$ contents decrease as the treatment



DOI: 10.1021/acs.inorgchem.5b01656
*Inorg. Chem.* 2015, 54, 9896−9907

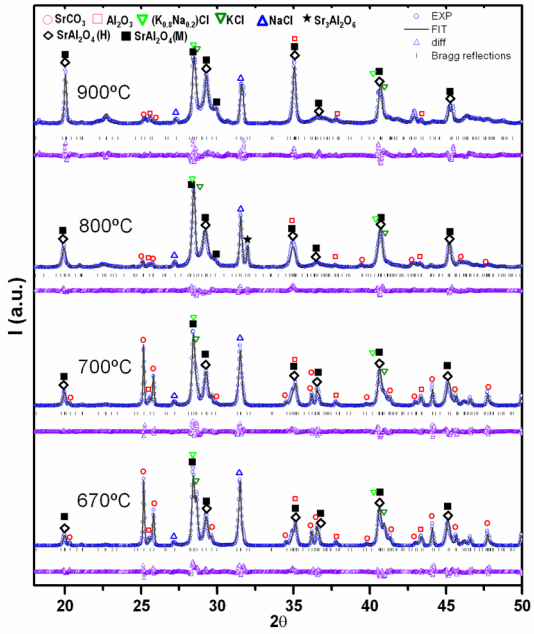


**Figure 5.** Rietveld refinement plots showing observed (circle blue line), calculated (continuous black line), and residual curves (triangle purple line) of powder diffraction data from samples heated at 670, 700, 800, and 900 °C for 1 h. The vertical bars denote Bragg reflection positions. The symbols highlight $SrCO_3$ (open red circles), $Al_2O_3$ (red open squares), NaCl (green open triangles), KCl (green open triangles), $(K_{0.8}Na_{0.2})Cl$ (bright green open circles), $SrAl_2O_4$ (hexagonal) (black open diamonds), and $SrAl_2O_4$ (monoclinic) (black squares).

temperature is increased, ranging from 15.9 wt % at 670 °C to 2.0 wt % at 900 °C for $SrCO_3$ and from 16.9 wt % at 670 °C to 8.9 wt % at 900 °C for $Al_2O_3$. These results are in agreement with the behavior observed by Raman spectroscopy in which the reduction of the $SrCO_3$ is almost complete for 800 °C, but some unreacted $Al_2O_3$ phase remains up to 900 °C.

The intensity of the XRD peaks of the salt decreases with increasing temperature, due to its vaporization during the thermal treatment, in good agreement with the DSC analysis. Concerning the $SrAl_2O_4$ crystalline phase, it is important to emphasize that the monoclinic pattern overlaps the hexagonal one, and therefore it is not be possible to make an accurate phase assignment. The monoclinic $SrAl_2O_4$ phase (space group $P2_1$) shows a pattern characterized by three peaks centered at 28.38°, 29.27°, and 29.92° ($2\theta$), whereas the $SrAl_2O_4$ hexagonal phase (space group $P6_322$) exhibits a main peak at $2\theta = 29.06°$. At 670 °C, the incipient $SrAl_2O_4$ hexagonal phase appears. It was previously reported that low contents of $Ca^{2+}$,[56] $Ba^{2+}$,[57] or $Al^{3+}$[58] excess can stabilize the hexagonal polymorph at room temperature. Given that an unreacted fraction of $Al_2O_3$ is present in this molten salt method, an excess of $Al^{3+}$ could be considered. However, the presence of locally unreacted $Al_2O_3$ seems to be related to the kinetics of the reaction and is most probably acting against the stabilization of the hexagonal phase. The XRD patterns show a shoulder at 29.93° ($2\theta$), which belongs to the monoclinic phase. At 670 °C, the amounts of hexagonal and monoclinic phases are 14.0 and 2.9 wt %, respectively. The amount of hexagonal phase increases from 15.8 to 25.5 wt % and the amount of monoclinic from 6.1 to 17.3 wt % for the sample treated at 700 and 800 °C, respectively. Furthermore, a secondary phase was identified at 800 °C; the indexation of these peaks reveals the formation of $Sr_3Al_2O_6$. The amount of $Sr_3Al_2O_6$ determined after Rietveld refinement is ca. 3.6% wt. *In situ* HT XRD confirmed that $Sr_3Al_2O_6$ is formed above 700 °C. However, this phase was not observed during the Raman study. Most probably, the intensity of the characteristic band located at 746 $cm^{-1}$ (see Supporting Information, Figure S1) and corresponding to $Sr_3Al_2O_6$ has a lower signal than other phases in the system; therefore it has not been possible to observe this Raman mode. The absence of this phase in the XRD pattern of the powder heated at 700 °C for 1 h suggests that holding time allows better diffusion during the reaction. However, at 800 °C both complete decomposition of $SrCO_3$ and decrease of the liquid viscosity favor the diffusion of $Sr^{2+}$ and therefore the appearance of secondary phases. Quantitative results show also that the hexagonal phase prevails at 800 °C, but the excess of $Al^{3+}$ localized in unreacted $Al_2O_3$ induces the formation of $Sr_3Al_2O_6$. Above 900 °C, the absence of $Sr_3Al_2O_6$ accounts for the diffusion of $Sr^{2+}$ from the Sr-rich aluminate phase to form $SrAl_2O_4$.

As expected, both the temperature and the holding time influence significantly the reaction mechanism. The monoclinic phase is the main phase at 900 °C when the incorporation of a higher amount of $Al_2O_3$ occurs. This result reveals that thermal treatments at lower temperatures promote secondary phases given the limitation of both the decomposition of the strontium carbonate and the reactivity of the alumina particles. The crystallinity of the monoclinic polymorph increases with the duration of the thermal treatment, which could be associated with particle growth. Moreover, a remarkable aspect is that this effect is also correlated with the evaporation of the salt. The results of the quantitative phase analysis took into account the presence of the different NaCl, KCl, and $(K_{0.8}Na_{0.2})Cl$ phases. The total amount of the salt decreases, ranging from 50.3 wt % at 670 °C to 41.1 wt % at 900 °C. The quantity of the $(K_{0.8}Na_{0.2})Cl$ solid solution decreases significantly, with amounts of 11.3 and 8.43 wt % for the samples treated at 670 and 700 °C, respectively. The amount of $(K_{0.8}Na_{0.2})Cl$ finally almost disappears (1 wt % at 800 and 900 °C). These data indicated that the extension of a eutectic salt is restricted by a preferential vaporization.

To sum up, the coexistence at room temperature of both monoclinic and hexagonal phases is stated, but there is no

**Table 1. Quantitative Weighted Amounts of Each Phase and Convergence *R* Factors (Figures-of-Merit) and $\chi^2$ and $R(F^2)$(%) Goodness-of-Fit Index Obtained by Refined Data of Diffractograms of the Powders Thermally Treated at 670, 700, 800, and 900 °C for 1 h**

| sample | $SrAl_2O_4$ H (wt %) | $SrAl_2O_4$ M (wt %) | $Sr_3Al_2O_6$ (wt %) | $SrCO_3$ (wt %) | $Al_2O_3$ (wt %) | salt (wt %) | Rwp (%) | $\chi^2$ | $R(F^2)$ (%) |
|---|---|---|---|---|---|---|---|---|---|
| 670 °C | 14.0 (2) | 2.9 (3) | | 15.9 (2) | 16.9 (4) | 50.3 (3) | 20.19 | 49.8 | 7.22 |
| 700 °C | 15.8 (3) | 6.1 (4) | | 14.2 (2) | 14.8 (4) | 49.0 (3) | 15.59 | 16.7 | 4.93 |
| 800 °C | 25.5 (4) | 17.3 (6) | 3.6 (1) | 2.3 (1) | 8.7 (4) | 42.6 (2) | 14.51 | 16.6 | 4.82 |
| 900 °C | 9.7 (1) | 42.5 (5) | | 2.0 (4) | 8.9 (9) | 41.1 (3) | 13.5 | 16 | 4.21 |



DOI: 10.1021/acs.inorgchem.5b01656
*Inorg. Chem.* 2015, 54, 9896−9907

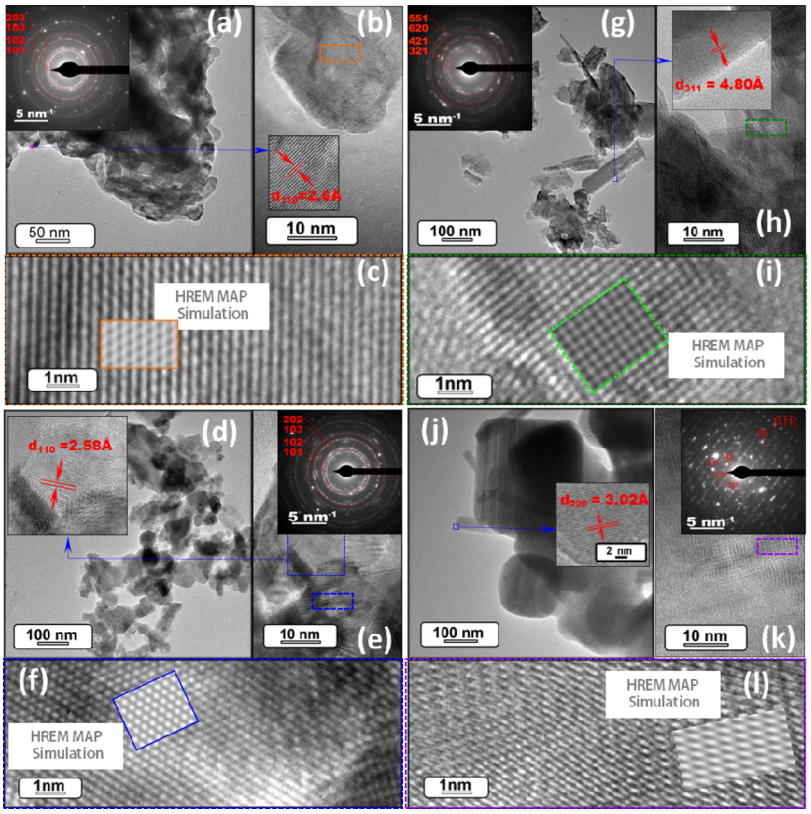


**Figure 6.** Low- and high-resolution TEM images of the powders thermally treated at 670 (a, b), 700 (d, e), 800 (g, h), and 900 °C (j, k) for 1 h. SAED patterns are shown as insets in panels a, e, g, and k for powders heated at 670, 700, 800, and 900 °C for 1 h, respectively. The rings are indexed based on the $SrAl_2O_4$ (H) (inset in panel a), $SrAl_2O_4$ (H) (inset in panel e), and $Sr_2Al_3O_6$ (inset in panel g) structures. The SAED patterns (k) can be indexed as oriented along the [−1−11] zone axis of the $SrAl_2O_4$ (M) structure. In (c), (f), (i), and (l) the image simulations are compared with experimental images of the selected area of HRTEM images for the powders thermally treated at 670, 700, 800, and 900 °C for 1 h, respectively.

obvious explanation for the stabilization of the high-temperature phase. Therefore, there is a need to evaluate the microstructure aspects to answer this question.

**3.5. Microstructure Study by HRTEM.** In order to explain the stabilization of the $SrAl_2O_4$ high-temperature form (hexagonal symmetry) at room temperature, the microstructure aspect was evaluated. High-resolution transmission electron microscopy (HRTEM) was performed to obtain a detailed phase and morphological characterization. TEM and HRTEM analyses of the powder heated at 670 °C for 1 h are illustrated in Figure 6a–c. The low-magnification TEM image (Figure 6a) shows the presence of particles embedded in the melting phase. The HRTEM image shown Figure 6b reveals distinguishable lattice fringes at this temperature. The interplanar distance from the inset in Figure 6b is 2.60 Å, which can be assigned to the (110) plane of $SrAl_2O_4$. The selected area electron diffraction (SAED) pattern recorded at the former location reveals ring patterns containing bright spots, which confirm the presence of a crystalline phase in the sample (Figure 6a inset). The SAED pattern is indexed according to (101), (102), (103), and (220) reflections of the hexagonal phase of $SrAl_2O_4$, corresponding to 3.89, 3.08, 2.36, and 1.98 Å calculated *d*-spacing, respectively. The inset in Figure 6c shows a multislice simulated HRTEM image along the [213] direction. An excellent agreement between the simulated image and the experimental image is evident, which confirms the hexagonal symmetry. The dimension of the crystalline regions is lower than 10 nm, and irregular edges are observed.

At 700 °C, the particles are morphologically defined and there is less presence of the melting phase, as shown in the low-magnification TEM image (Figure 6d). The inset in Figure 6e shows the corresponding SAED pattern, which exhibits four rings, the *d*-spacing being calculated as 3.88, 3.09, 2.37, and 1.99 Å, corresponding to (101), (102), (103), and (220) reflections. Moreover, the good crystallinity is confirmed by the distinguishable lattice fringes in Figure 6e. The reflections correspond to the $SrAl_2O_4$ hexagonal phase. This finding is in agreement with the quantitative Rietveld refinement performed from powder XRD patterns, which indicates a major quantity of hexagonal phase at this temperature. The *d*(110) spacing measured in the inset of Figure 6d is in agreement with the value of 2.58 Å, which has to be expected from the hexagonal phase. The dimensions of this coherent crystalline region are still lower than 10 nm.

Figure 6g–i show a sequence of TEM and HRTEM images of the powder thermal treated at 800 °C for 1 h. The low-magnification TEM image shows the presence of two types of particles that have very different shapes. Some particles have similar morphology to the particles synthesized at 700 °C; the others have a tubular morphology, as shown in Figure 6h. The interplanar distance from the inset in Figure 6h was 4.80 Å, which can be associated with the (311) plane in $Sr_3Al_2O_6$. The SAED pattern (inset in Figure 6g) of the lattice fringes of the area selected (dashed green rectangle) in Figure 6h reveals ring patterns belonging to $Sr_3Al_2O_6$, the *d*-spacing being calculated as 4.20, 3.50, 2.53, and 2.20 Å, corresponding to (321), (421),



DOI: 10.1021/acs.inorgchem.5b01656
*Inorg. Chem.* 2015, 54, 9896–9907

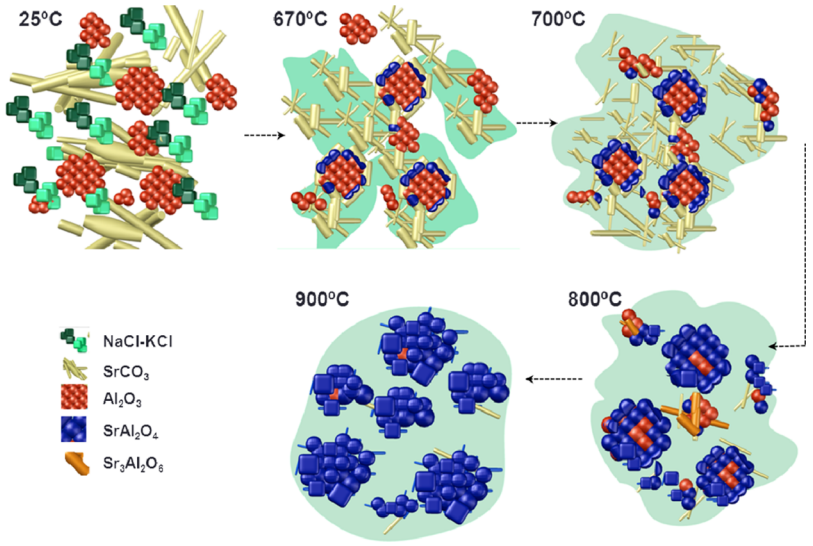


**Figure 7.** Reaction process scheme representing the $SrAl_2O_4$ formation mechanism. The first stage illustrates the raw materials at room temperature. The second stage exhibits the beginning of the reaction at 670 °C. The eutectic mixture turns into a molten state and surrounds the precursors, allowing a better diffusion between these components. Moreover, the breakup of strontium carbonate occurs. The third stage denotes the reaction at higher temperature (700 °C), which is characterized by a rise of the reaction. The fourth stage at 800 °C depicts two phenomena: the formation of the rod-like $Sr_2Al_3O_6$ particles promoted by a local excess of $SrCO_3$ and the growth of $SrAl_2O_4$. Finally the fifth stage at 900 °C shows the growth of $SrAl_2O_4$(M).

(621), and (551) reflections. This result demonstrates that the secondary phase found also by XRD has a different growth habit. Finally, TEM analyses (Figure 6j) of the powder treated at 900 °C consist of crystalline spherical particles; there is a clear increase of the particle size compared to thermal treatment at 700 and 800 °C. The $d$(220) spacing measured in the inset in Figure 6d is in agreement with the value of 3.02 Å related to the $SrAl_2O_4$ monoclinic phase. Further experimental proof of the higher crystallinity of this powder is shown by the HRTEM image and the related SAED pattern in Figure 6k and in the inset of Figure 6k, respectively. The diffraction spots can be indexed as the diffractions of a [−1−11] zone axis. The multislice simulation can be seen in the inset of Figure 6f, i, and l; the agreement between observations and simulations is reasonably good.

The stabilization at room temperature of the high-temperature hexagonal polymorph is thus related to the particle sizes that are obtained for lower temperatures. The stabilization of the high-temperature phase is common in other systems such as $BaTiO_3$, in which the reduction of the particle size preserves the cubic high-temperature phase.[59,60] The coexistence of hexagonal and monoclinic phases is a signature of the particle size obtained: when the amount of monoclinic phase grows, the particle size increases too. This result corroborates the red-shift of the Raman peak observed at 478 $cm^{-1}$ as an indication of the monoclinic phase formation. To keep nanometric crystalline domains in order to synthesize nanometer-scale particles, the approach that should be developed is stabilizing the hexagonal polymorph at room temperature. However, this strategy requires a detailed study taking into account that the monoclinic polymorph is stable below 650 °C, and there is no clear agreement on the emission of the hexagonal structure.[46,61]

**3.6. Reaction Mechanism Schematic Diagram.** In order to propose a reaction mechanism, a schematic model has been developed and is shown in Figure 7. The results of the previous observations have been taken into account and are depicted in the scheme. Regarding the $SrCO_3$ DSC-TG-DTG analysis, the presence of the salt appears fundamental to promote the decomposition of $SrCO_3$ and the diffusion of $Sr^{2+}$. On the other hand, Raman images show that at 670 and 700 °C the $SrCO_3$ is partially distributed, and there are located areas where the precursor is not decomposed. At higher temperature, powder XRD and Raman characterizations reveal that $SrCO_3$ is practically decomposed and reacts with $Al_2O_3$ at 800 and 900 °C. From XRD and Raman characterizations, we can state that unreacted $Al_2O_3$ remains at 800 and 900 °C in the presence of $SrAl_2O_4$ particles, but a core−shell structure was not found by TEM. In relation to the salt, the TG analysis of the $SrCO_3$ + $Al_2O_3$ + $(NaCl−KCl)_e$ system shows that the weight loss is around 20% at 900 °C, so it can be inferred that this loss is mainly related to the $SrCO_3$ decomposition, and a small contribution is due to the evaporation of the salt. A great quantity of salt remains present up to 900 °C, which corroborates the quantitative Rietveld refinement. The formation of the $Sr_2Al_3O_6$ secondary phase, detected by XRD in the sample heated at 800 °C for 1 h, can be attributed to a local excess of $SrCO_3$. By TEM analysis it has been observed that the morphology of this phase corresponds to a rod-like structure, as shown in Figure 7g. In addition, the presence of $Sr_2Al_3O_6$ has been observed for short dwell times of thermal treatments due to the lack of homogeneous diffusion of $Sr^{2+}$.

On the basis of the discussed results, a reaction mechanism of $SrAl_2O_4$ formation can be proposed. The first image presented in Figure 7 illustrates the raw materials at room temperature. The $SrCO_3$ particles have a rod-like structure (as shown in FE-SEM micrographs in Supporting Information Figure S2). The submicrometer $Al_2O_3$ particles are represented as agglomerates (red spheres). The salt mixture (NaCl−KCl) is symbolized by cubes (green light and green dark). The second scheme illustrates the reaction when it has reached 670 °C, a temperature above the melting point of the eutectic mixture (659 °C). The salt is partly in the molten state and creates a highly mobile environment. The presence of a liquid phase


DOI: 10.1021/acs.inorgchem.5b01656
Inorg. Chem. 2015, 54, 9896−9907

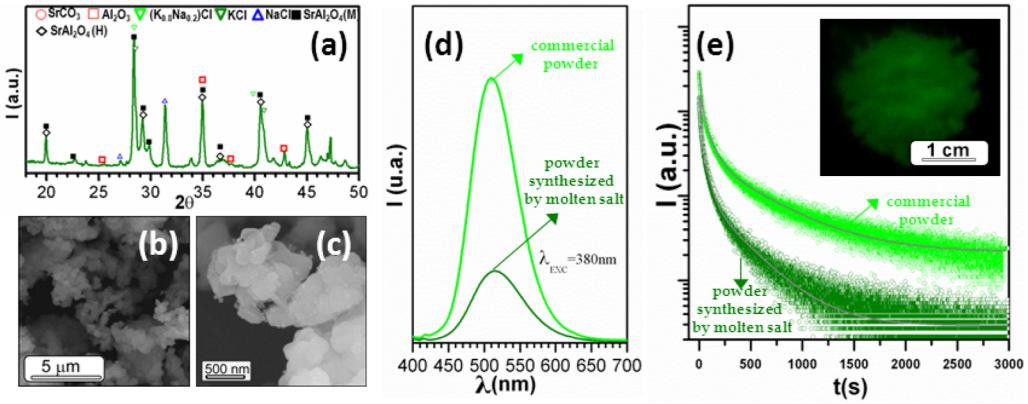


**Figure 8.** (a) XRD pattern of the $Sr_{0,97}Al_2O_4$:$Eu_{0,02}$, $Dy_{0,01}$ powder synthesized by molten salt at 900 °C for 1 h in a $N_2$–$H_2$ atmosphere. (b, c) FE-SEM micrographs. (d) Emission spectra upon excitation at 380 nm of (e) experimental (dotted line) and fitting (solid line) decay curves after excitation at 380 nm for 10 min. The inset shows a long-lasting phosphorescence image of the powder synthesized by molten salt.

produces two main effects: first the closeness of surrounding agglomerates due to the surface tension of the liquid and, second, the rearrangement of the agglomerates that produced disaggregation of $SrCO_3$ and $Al_2O_3$. In the case of molten salt synthesis, the formation of strontium aluminate is assisted by the liquid media and favored by the decomposition of the $SrCO_3$ particles. The hexagonal polymorph is formed (blue spheres) because it is the stable structure at this temperature. Increasing the temperature to 700 °C leads to a more pronounced decomposition of $SrCO_3$, as observed in the third scheme; likewise the formation of strontium aluminate increases. The fourth scheme gives evidence of the phenomenology effect observed at 800 °C: the massive decomposition of $SrCO_3$ promotes the appearance of both $SrAl_2O_4$ and $Sr_2Al_3O_6$ crystalline phases. At the final stage of the reaction mechanism (900 °C), the particle growth favors the formation of more equiaxial particles that transform to monoclinic phase during cooling. The remaining raw materials and crystallized salt are characteristic of the reaction mechanism. Employing a reactive alumina with a particle size smaller than 0.5 μm, the reaction rate is much larger than that developed in the solid-state method, showing that dissolution/precipitation dominates over the dissolution–diffusion transport mechanism ("template mechanism").

**3.7. Photoluminescence Response.** $SrAl_2O_4$ is a well-known and attractive matrix that exhibits strong persistent luminescence properties when doped by $Eu^{2+}$ and $Dy^{3+}$.[62] However, the phosphor powders currently produced by different synthetic routes have a wide particle size range, between 20 and 100 μm, that limited their use in applications that require fine powder, such as printing. A method for reducing the particle size has not yet been developed; nevertheless our previous results of synthesis in an air atmosphere point out that submicrometer particles of $SrAl_2O_4$ can be obtained by molten salt synthesis. In order to obtain a phosphorescence response, europium and dysprosium have been incorporated as dopants to our system to synthesize $SrAl_2O_4$:$Eu^{2+}$, $Dy^{3+}$ materials. The powders were thermally treated at 900 °C for 1 h in a furnace under a nitrogen–hydrogen ($90N_2$–$10H_2$) atmosphere to reduce $Eu^{3+}$ to $Eu^{2+}$.

As shown in Figure 8a, the XRD pattern of the powder thermally treated at 900 °C for 1 h is similar to the powder treated in air. The presence of residual salt is not a limiting factor to obtain functional properties. Moreover, taking into account the results of TG analyses, the salt starts to vaporize above the melting point (659 °C); therefore the salt can be eliminated during the synthesis process by evaporation. Eu and Dy cations have not been detectable on the XRD; therefore a low doping concentration does not alter the crystal structure. The crystallite size ($D$) of the powders can be estimated from the full width at half-maximum of the diffraction peak by Scherer's equation:

$$D = \frac{K\lambda}{B\cos\theta} \quad (1)$$

where $\lambda$ is the X-ray wavelength, $B$ is the half-maximum of the diffraction peak, and $\theta$ is the angle of diffraction, using a shape factor ($K$) of 0.9. The indexed diffraction peaks (−221), (220), (211), and (031) for the monoclinic phase are selected to calculate the crystallite size. A crystallite size of ca. 34 nm has been obtained. The FE-SEM micrographs shown in Figure 8b,c, illustrate the morphology of the powders. From Figure 8b,c, it can be observed that the powders are composed of small plate-like particles with sizes of 50–200 nm that form strongly bound agglomerates with sizes of ∼3 μm.

The main optical response of the $Sr_{0,97}Al_2O_4$:$Eu_{0,02}$, $Dy_{0,01}$ powder is presented in Figure 8d,e. The measurements are compared to a commercial powder (from Jinan Chenghao Technology Co., Ltd.). The commercial powder has been milled by the dry milling process to reduce the particle size, obtaining an average particle size, $d_{50}$, of ∼4 μm.[63] This powder has been chosen to compare the properties with a powder showing a particle size as small as possible. This powder was obtained by carefully controlling the milling duration to avoid amorphization of the particles in order to retain PL properties.[63] This approach allows comparing the functional properties with the powder synthesized by molten salt, which has an average agglomerate size of ca. 3 μm. Figure 8d shows the photoluminescence emission spectrum ($\lambda_{exc}$ = 380 nm) of $Sr_{0,97}Al_2O_4$:$Eu_{0,02}$, $Dy_{0,01}$ powder compared to the commercial powder. The emission band centered at 510 nm is assigned to the transition $4f^65d^1 \rightarrow 4f^7$ ($^8S_{7/2}$) of $Eu^{2+}$ ions.[64] Figure 8e shows the decay curve of the phosphorescence of the powders synthesized. The intensity of the emission of the powder synthesized by molten salt is lower than the intensity of the commercial powder; however it should be taken into account that the commercial powder has a micrometer size, while the powder synthesized by molten salt is submicrometer. It is known that nanosized $SrAl_2O_4$:$Eu^{2+}$, $Dy^{3+}$ phosphors show


DOI: 10.1021/acs.inorgchem.5b01656
Inorg. Chem. 2015, 54, 9896–9907

Table 2. Fitting Results of the Decay Parameters

| sample | $I_1$ | $A_1$ | $\tau_1$ | $A_2$ | $\tau_2$ | $A_3$ | $\tau_3$ |
|---|---|---|---|---|---|---|---|
| commercial powder milled | 215(1) | 14 788(44) | 15.60(1) | 10 476(40) | 77.9(3) | 2731(14) | 509(2) |
| powder synthesized by molten slats | 29(1) | 7835(16) | 11(1) | 5359(18) | 53(1) | 1007(6) | 327(2) |

lower intensity and shorter persistent time compared with microsized phosphors.[65,66] Moreover, the afterglow has been evaluated. The powder was previously irradiated for 10 min at 380 nm. After the light source was cut off, the phosphorescent decay was measured. The phosphorescent decay time follows an exponential law. The decay curves are usually fitted by the sum of two exponential components ($I = A_1 \exp(-t/\tau_1) + A_2 \exp(-t/\tau_2)$). However, if more independent traps exist, the equation can be rewritten as a multiple exponential equation and can include a supplementary term, the final intensity, to obtain better accuracy.[67] Decay curves can be fitted using the following equation:

$$I = I_1 + A_1 \exp\frac{-t}{\tau_1} + A_2 \exp\frac{-t}{\tau_2} + A_3 \exp\frac{-t}{\tau_3} \quad (2)$$

where $I_1$ is the final intensity; $A_1$, $A_2$, and $A_3$ are constants; $t$ is the decay time; and $\tau_1$, $\tau_2$, and $\tau_3$ are fitting parameters related to the decay rate of the phosphor. The fitting results of the parameters are compiled in Table 2. Although the powder synthesized shows a lower emission and afterglow initial intensity than the commercial counterpart, the reduction is less than the drop reported by Tang et al.,[20] which decreases by 1 order of magnitude. Therefore, the results presented here can be considered as a promising achievement and demonstrate a clear advantage of the molten salt method proposed. The photoluminescence emission of the powders is also macroscopically apparent; the inset in Figure 8d shows a photograph of the resultant powders emitting green phosphorescence after the UV illumination has been cut off.

In summary, the large size of the commercial powders is a major drawback for the practical applications of $SrAl_2O_4$-based materials such as printing applications. As a result, the synthesis and design of $SrAl_2O_4$:$Eu^{2+}$, $Dy^{3+}$ phosphors by the molten salt method has become an efficient way to further enhance the particle size and suitable photoluminescence response of $SrAl_2O_4$ materials, narrowing the gap between submicrometer phosphors and their commercial analogues of micrometer size.

## 4. CONCLUSIONS

$SrAl_2O_4$ has been successfully synthesized by the molten salt method using the $(NaCl-KCl)_e$ eutectic mixture as molten flux. The use of this innovative process induces an increase in the reaction rate and a reduction of the formation temperature of $SrAl_2O_4$ in comparison with the classic solid-state method. Through this study, we have elucidated the reaction mechanism of strontium aluminate formation assisted by $(NaCl-KCl)_e$. $SrCO_3$ decomposes in the eutectic salt, allowing strong diffusion in the system. As a consequence, the formation of $SrAl_2O_4$ is favored at low temperatures. The reaction mechanism is developed by taking into account the effects of dissolution−precipitation and diffusive matter transport through the liquid phase. The dissolution−precipitation contribution is dominant employing a reactive alumina.

In order to obtain high-quality $SrAl_2O_4$ powders, it is usually necessary to use high annealing temperatures and long reaction times. The synthetic approach presented here provides the conditions to achieve high crystallinity in submicrometer particles, as observed by HRTEM and XRD, and offers a potentially scalable process. Moreover, the molten salt synthesis technique could be employed for a wide range of materials based either on strontium aluminate or on other material compositions. Persistent luminescence properties have been demonstrated for $SrAl_2O_4$ samples doped with $Eu^{2+}$ and $Dy^{3+}$ and heated at 900 °C for 1 h. On account of these results, it is expected that the molten salt route proposed here could offer a straightforward alternative method for the synthesis of technologically relevant phosphorescent powders.

## ■ ASSOCIATED CONTENT

### Supporting Information

The Supporting Information is available free of charge on the ACS Publications website at DOI: 10.1021/acs.inorgchem.5b01656.

XRD and Raman spectroscopy characterization of the $Sr_3Al_2O_6$ structure and FE-SEM micrographs of $SrCO_3$ and $Al_2O_3$ (PDF)

## ■ AUTHOR INFORMATION


### Corresponding Author

*Tel: +34 91 735 58 40, ext. 1074. Fax: +34 91 735 58 43. E-mail: rociorojas@icv.csic.es (R. E. Rojas-Hernandez).


### Notes

The authors declare no competing financial interest.

## ■ ACKNOWLEDGMENTS


The authors express their thanks to the MINECO (Spain) project MAT2013-480089-C04-1-P for their financial support. R.E.R-H. is grateful to Ibero-America Young Teachers and Researchers programme-Santander grants for a short stay scholarship. R.E. R-H. acknowledges use of the facilities of the Prof. Dr. Edson Leite Group (Chemistry Department at Federal University of Sao Carlos (UFSCar), SP, Brazil). F.R.-M. is also indebted to MINECO for a "Juan de la Cierva" contract (ref: JCI-2012-14521), which is cofinanced with European Social Fund.


## ■ REFERENCES


(1) Palilla, F. C.; Levine, A. K.; Tomkus, M. R. *J. Electrochem. Soc.* **1968**, *115*, 642−644.
(2) Abbruscato, V. *J. Electrochem. Soc.* **1971**, *118*, 930−933.
(3) Aitasalo, T.; Dereń, P.; Hölsä, J.; Jungner, H.; Krupa, J.-C.; Lastusaari, M.; Legendziewicz, J.; Niittykoski, J.; Stręk, W. *J. Solid State Chem.* **2003**, *171*, 114−122.
(4) Hölsa, J.; Jungner, H.; Lastusaari, M.; Niittykoski, J. *J. Alloys Compd.* **2001**, *324*, 326−330.
(5) Yina, H.; Xinye, J.; Qiang, C.; Ding, L.; Farong, W. *J. Rare Earths* **2006**, *24*, 157−159.
(6) Karasu, B.; Kaya, S. Y. *Ceram. Int.* **2012**, *38*, 2757−2766.
(7) Van Duynhoven, D. M. Tintable luminescent paint. Patent CA2309871, August 19, 2003.
(8) Pet, R. J.; Van der Nienwenhof, M.; Duisters, J. P. H. M. Method of preparing a luminescent $Eu^{2+}$ activated strontium aluminate. U.S. Patent 4795588 (A), January 3, 1989.




DOI: 10.1021/acs.inorgchem.5b01656
*Inorg. Chem.* 2015, 54, 9896−9907

(9) Escribano, P.; Marchal, M.; Luisa Sanjuán, M.; Alonso-Gutiérrez, P.; Julián, B.; Cordoncillo, E. *J. Solid State Chem.* **2005**, *178*, 1978−1987.
(10) Qiu, Z.; Zhou, Y.; Lu, M.; Zhang, A.; Ma, Q. *Acta Mater.* **2007**, *55*, 2615−2620.
(11) Lin, Y.; Zhang, Z.; Zhang, F.; Tang, Z.; Chen, Q. *Mater. Chem. Phys.* **2000**, *65*, 103−106.
(12) Yu, X.; Zhou, C.; He, X.; Peng, Z.; Yang, S. *Mater. Lett.***2004**, *58*, 1087−109110.1016/j.matlet.2003.08.022.
(13) Rojas-Hernandez, R. E.; Rodriguez, M. a.; Fernandez, J. F. *RSC Adv.* **2015**, *5*, 3104−3112.
(14) Rojas-Hernandez, R. E.; Rodriguez, M. a.; Rubio-Marcos, F.; Serrano, a.; Fernandez, J. F. *J. Mater. Chem. C* **2015**, *3*, 1268−1276.
(15) Li, Z.; Zhang, Y.; Wu, X.; Wu, X.; Maudgal, R.; Zhang, H.; Han, G. *Adv. Sci.* **2015**, *2*, n/a.
(16) Luo, X.; Cao, W.; Xiao, Z. *J. Alloys Compd.* **2006**, *416*, 250−255.
(17) Song, Y. K.; Choi, S. K.; Moon, H. S.; Kim, T. W.; Mho, S.-I.; Park, H.LK. *Mater. Res. Bull.* **1997**, *32*, 337−341.
(18) Sanchez-Benitez, J.; de Andrés, A.; Marchal, M.; Cordoncillo, E.; Regi, M. V.; Escribano, P. *J. Solid State Chem.* **2003**, *171*, 273−277.
(19) Li, Z.; Zhang, Y.; Wu, X.; Huang, L.; Li, D.; Fan, W.; Han, G. *J. Am. Chem. Soc.* **2015**, *137*, 5304−5307.
(20) Tang, Z.; Zhang, F.; Zhang, Z.; Huang, C.; Lin, Y. *J. Eur. Ceram. Soc.* **2000**, *20*, 2−5.
(21) Kimura, T. *Advances in Ceramics - Synthesis and Characterization, Processing and Specific Applications*; Sikalidis, C., Ed.; InTech, 2011.
(22) Lallart, M. *Ferroelectrics - Material Aspects- Synthesis of Ferroelectric Na0.5Bi0.5TiO3 by MSS (Molten Salt Synthesis) Method*; InTech, 2010.
(23) Zhou, H.; Mao, Y.; Wong, S. S. *Chem. Mater.***2007**, *19*, 5238−524910.1021/cm071456j.
(24) Liu, L.; Gao, F.; Hu, G.; Liu, J.; Li, J. *J. Alloys Compd.* **2013**, *580*, 93−100.
(25) Li, Z.; Zhang, S.; Lee, W. E. *J. Eur. Ceram. Soc.* **2007**, *27*, 3407−3412.
(26) Wasserscheid, P. *Nature* **2006**, *439*, 797.
(27) Ewing, C. T.; Stern, K. H. *J. Phys. Chem.* **1974**, *78*, 1998−2005.
(28) Taş, A. *J. Am. Ceram. Soc.* **2001**, *84*, 295−300.
(29) Aydogan, E.; Kaya, S.; Dericioglu, A. F. *Ceram. Int.* **2014**, *40*, 2331−2336.
(30) García-Guaderrama, M.; Arizaga, G. G. C.; Durán, a. *Ceram. Int.* **2014**, *40*, 7459−7465.
(31) Jiang, H.; Wang, X.; Wang, L.; Yu, C.; Mu, J. *Mater. Manuf. Processes* **2013**, *28*, 336−340.
(32) Vradman, L.; Zana, J.; Kirschner, A.; Herskowitz, M. *Phys. Chem. Chem. Phys.* **2013**, *15*, 10914−10920.
(33) Afanasiev, P.; Afanasiev, P.; Geantet, C.; Geantet, C. *Coord. Chem. Rev.* **1998**, *180*, 1725−1752.
(34) Jayaseelan, D. D.; Zhang, S.; Hashimoto, S.; Lee, W. E. *J. Eur. Ceram. Soc.* **2007**, *27*, 4745−4749.
(35) Dreele, R.; Von Larson, A. *General structure analysis system (GSAS)*; Los Alamos National Laboratory Report, 2004.
(36) Toby, B. H. *J. Appl. Crystallogr.* **2001**, *34*, 210−213.
(37) Taylor, D. *Br. Ceram. Proc.* **1984**, *83*, 92−98.
(38) Cowley, J. M.; Moodie, a. F. *Acta Crystallogr.* **1957**, *10*, 609−619.
(39) Stadelmann, P. *EMS Java Versión*, CIME-EPFI, CH1015, Lausanne, Switzerland, 2004.
(40) Pelton, A. D.; Gabriel, A.; Sangster, J. *J. Chem. Soc., Faraday Trans. 1* **1985**, *81*, 1167−1172.
(41) Kelkar, M. S.; Maginn, E. J. *J. Phys. Chem. B***2007**, *111*, 9424−942710.1021/jp073253o.
(42) Chang, Y.; Hsiang, H.; Liang, M. *J. Am. Ceram. Soc.* **2007**, *90*, 2759−2765.
(43) Dobrovinskaya, E. R. Lytvynov, L. A.; Pishchik, V. *Sapphire: Material, Manufacturing, Applications*; Springer: New York, 2009.
(44) Zaki, M. I.; Hussien, G. A. M.; Fahim, R. B. *J. Therm. Anal.* **1985**, *30*, 129−134.
(45) Nag, A.; Kutty, T. R. N. *J. Alloys Compd.* **2003**, *354*, 221−231.
(46) Cordoncillo, E.; Julian-Lopez, B.; Martínez, M.; Sanjuán, M. L.; Escribano, P. *J. Alloys Compd.* **2009**, *484*, 693−697.
(47) Kastler, A.; Rousset, A. *J. Phys. Radium* **1941**, *2*, 49−57.
(48) Buzgar, N.; Apopei, A. *The Raman Study of Certain Carbonates*; Analele Stiintifice Ale Universitatii: Al. I. Cuza Iasi Geologie, 2009; Vol. *55*, pp 97−112.
(49) Kastler, A.; Rousset, A. *J. Phys. Radium* **1941**, *2*, 49.
(50) Krishnan, T. S. *Proc. Indian Acad. Sci.* **1956**, *44*, 96−98.
(51) Porto, S. P. S.; Krishnan, R. S. *J. Chem. Phys.* **1967**, *47*, 1009.
(52) Raptis, C. *Phys. Rev. B: Condens. Matter Mater. Phys.* **1986**, *33*, 15−17.
(53) Krantz, M.; Luty, F. *Phys. Rev. B: Condens. Matter Mater. Phys.* **1985**, *31*, 2599−2601.
(54) Cordoncillo, E.; Julian-lopez, B.; Martínez, M.; Sanjuan, M. L. *J. Alloys Compd.* **2009**, *484*, 693−697.
(55) Young, R. A.; Wiles, D. B. *J. Appl. Crystallogr.* **1982**, *15*, 430−438.
(56) Prodjosantoso, A. K.; Kennedy, B. J. *J. Solid State Chem.* **2002**, *168*, 229−236.
(57) Henderson, C. M. B. *Mineral. Mag.* **1982**, *45*, 111−127.
(58) Douy, A.; Capron, M. *J. Am. Ceram. Soc.* **2002**, *85*, 3036−3040.
(59) Lambeck, P. V.; Jonker, G. H. *Ferroelectrics* **1978**, *22*, 729−731.
(60) Criado, J. M.; Dianez, M. J.; Gotor, F. J. *Ferroelectr., Lett. Sect.* **1992**, *14*, 79−84.
(61) Dong-Dong, J.; Bo-Qun, W.; Jing, Z. *Chin. Phys.* **2000**, *9*, 69.
(62) Matsuzawa, T.; Aoki, Y.; Takeuchi, N.; Murayama, Y. *J. Electrochem. Soc.* **1996**, *143*, 2670.
(63) Rojas-Hernandez, R. E.; Rubio-Marcos, F.; Enríquez, E.; De La Rubia, M. A.; Fernandez, J. F. *RSC Adv.* **2015**, *5*, 42559−42567.
(64) Clabau, F.; Rocquefelte, X.; Jobic, S.; Deniard, P.; Whangbo, M.; Garcia, A.; Rouxel, J. *Chem. Mater.* **2005**, *17*, 3904−3912.
(65) Kshatri, D. S.; Khare, A. *J. Lumin.* **2014**, *155*, 257−268.
(66) Geng, J.; Wu, Z. *J. Mater. Synth. Process.* **2002**, *10*, 245−248.
(67) Jiang, T.; Wang, H.; Xing, M.; Fu, Y.; Peng, Y.; Luo, X. *Phys. B* **2014**, *450*, 94−98.


DOI: 10.1021/acs.inorgchem.5b01656
*Inorg. Chem.* 2015, 54, 9896−9907